Research Article

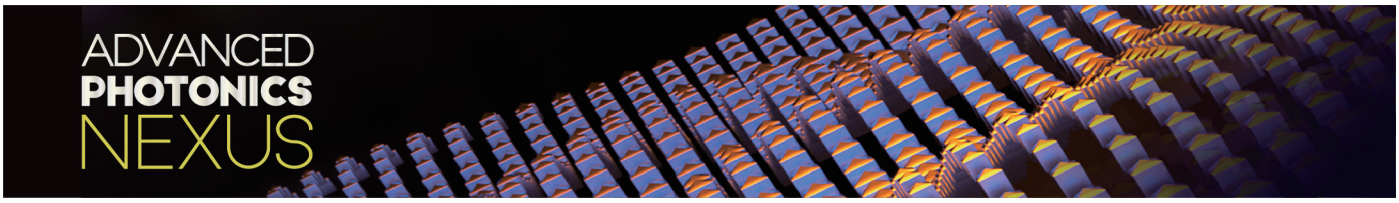

Terahertz vortices with tunable topological charges from a laser–plasma channel

Linzheng Wang,[a,b] Yanping Chen,[a,b,*] Chen Wang,[a,b] Huanyu Song,[a,b] Jinyu Hua,[a,b] Rong Huang,[a,b] Min Chen,[a,b] Jie Zhang,[a,b,c] and Zhengming Sheng[a,b,c,*]

[a]Shanghai Jiao Tong University, School of Physics and Astronomy, Key Laboratory for Laser and Plasma (MOE), Shanghai, China
[b]Shanghai Jiao Tong University, Collaborative Innovation Centre of IFSA, Shanghai, China
[c]Tsung-Dao Lee Institute, Shanghai, China

Abstract. Fractional optical vortices in the terahertz (THz) regime are supposed to have unique applications in various areas, i.e., THz communications, optical manipulations, and THz imaging. However, it is still challenging to generate and manipulate high-power THz vortices. Here, we present a way to generate intense THz vortex beams with a continuously tunable topological charge by injecting a weakly relativistic ultrashort laser pulse into a parabolic plasma channel. By adjusting the injection conditions of the laser pulse, the trajectory of the laser centroid can be twisted into a cylindrical spiral, along which laser wakefields are also excited. Due to the inhomogeneous transverse density profile of the plasma channel and laser wakefield excitation, intense THz radiation carrying orbital angular momentum is produced with field strength reaching sub-GV/m, even though the drive laser energy is at a few tens of mJ. The topological charge of such a radiation is determined by the laser trajectories, which are continuously tunable as demonstrated by theoretical analysis as well as three-dimensional particle-in-cell simulations. Such THz vortices with unique properties may find applications in broad areas.

Keywords: terahertz; optical vortex; laser–plasma interaction.

Received Jan. 8, 2025; revised manuscript received Feb. 21, 2025; accepted for publication Mar. 14, 2025; published online Apr. 11, 2025.

[DOI: 10.1117/1.APN.4.3.036004]

1 Introduction

Optical vortices with a helical wavefront around the phase singularity and a doughnut-shaped intensity profile bring a new degree of light beams, i.e., orbital angular momentum (OAM). The unique physical properties of optical vortices have facilitated applications including optical manipulations of matters,[1,2] communications,[3,4] quantum entanglement,[5,6] and high-resolution imaging.[7,8] Nowadays, optical vortices can be produced even with fractional topological charge,[9] which have attracted enormous attention in many fields owing to their unusual properties.[10,11] First, the fractional vortices featuring radially opening rings enable fine manipulations on particles or cells, i.e., transporting[12] and controlled rotating.[13] Subsequently, as fractional vortices can be decomposed into a series of integer vortices, it has been proven to improve the capacity of communications.[14] Moreover, fractional vortices may be helpful in edge enhancement of optical imaging[15,16] and analyzing some physical processes, i.e., high-dimensional quantum entanglement[17] and fractional flux quantum vortices in superconductors.[18]

On the other hand, the generation and application of vortices in the terahertz (THz) band have attracted increasing interest as it covers characteristic frequencies of many physical processes,[19] rotational and vibrational energy levels of many molecules,[20] and the near-future communication bands as well.[21] Heretofore, THz vortices have already been employed to manipulate non-linearities in graphene,[22] Bose–Einstein condensation currents,[23] and biological macromolecules.[24] In addition, THz vortices are found to be capable of reshaping electron bunches.[25] Possible ways to generate THz vortices are to modulate the wavefronts of the THz beams by use of spiral phase plates,[26] q-plates,[27] or some diffractive optical elements.[28,29]

*Address all correspondence to Yanping Chen, yanping.chen@sjtu.edu.cn; Zhengming Sheng, zmsheng@sjtu.edu.cn

However, it is not possible to tune the topological charge flexibly with fractional topological charges. Laser–plasma-based schemes are supposed to produce intense THz vortices with high tunability. For instance, THz vortices were generated from long plasma filaments excited with two-color optical vortices.[30,31] Besides, the interaction between optical vortices and spatially modulated plasmas may also lead to THz vortices.[32] However, these laser–plasma schemes require complex manipulations both on the topological charges of the input lasers and the plasma structures. In general, there is a lack of effective means to generate THz vortices with tunable topological charges up to now.

Here, we present a way to generate intense THz radiation with continuously tunable topological by non-collinearly injecting a femtosecond laser pulse into a parabolic plasma channel. By adjusting the injection condition of the laser pulse, the trajectory of the laser centroid can be twisted into a cylindrical spiral with a constant radius. In this case, the laser ponderomotive force induces net currents in the radial direction. Due to the propagation effects of both THz radiation and laser pulses, the THz radiation at far field features with phase gradients wrapping around the propagation direction, leading to a THz vortex. By conducting three-dimensional (3D) particle-in-cell (PIC) simulations, it is proved that the topological charge of the THz radiation can be continuously tunable by only adjusting the injection conditions of the laser pulses. As the required laser pulses are only at the weakly relativistic level with the pulse energy of a few tens of mJ and the plasma channel can be produced with existing techniques, this plasma-based high-power THz vortex source can be realized with existing technologies.

2 Results

2.1 Laser Propagation Inside a Plasma Channel

It was demonstrated previously that ultrashort laser pulses can be well-guided in parabolic plasma channels with the plasma density profile $n(r) = n_0 + \Delta n r^2/r_0^2$.[33,34] Here, Δn and r_0 are respectively the depth and width of the plasma channel. Once the laser pulse is non-collinearly injected into the channel, the trajectory of the laser beam centroid is a spiral around the channel axis.[35] We notice that the beam centroid rotates in a cylindrical spiral with a fixed radius if the injection condition for the laser pulse meets $z_0 \cos\theta_z = y_0 \cos\theta_y$, where θ_y and θ_z are the angles between the injection direction and the coordinate axes y and z, respectively (see the Supplementary Material). The coordinate (y_0, z_0) is defined as the location of the laser pulse at the entrance of the plasma channel (or the vacuum–channel boundary). Therefore, the laser pulse can pass through a parabolic plasma channel in a cylindrical spiral with an injection condition of $y_0 = 0$ and $\theta_z = \pi/2$ with varied z_0 and θ_y, as shown in Fig. 1(a). We keep this laser injection condition hereafter for convenience. In this case, the corresponding propagation period $\Lambda_0 = 2\pi|z_0 \tan\theta_y|$, which is completely determined by z_0 and θ_y. Meanwhile, the chirality

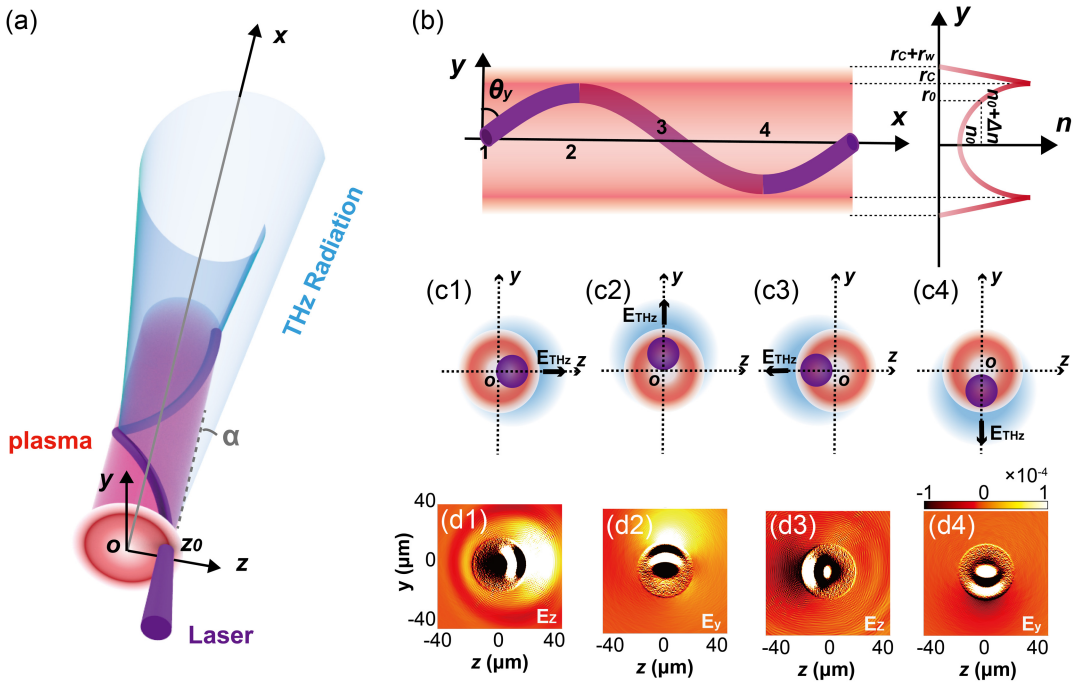

Fig. 1 Schematic of THz radiation in a parabolic plasma channel. (a) Schematic of the laser trajectory in a cylindrical spiral along the channel and the generated conical THz radiation with an open angle of 2α. (b) Illustration of the laser injection conditions from the side view in the x-y plane with an initial offset distance on the z-axis and the transverse density profile of the plasma channel. (c) Transverse distributions of the THz radiation at different positions along the x-axis at $x = 0, \Lambda_0/4, \Lambda_0/2, 3\Lambda_0/4$ as marked in panel (b). (d) Snapshots of the transverse electric field associated with the THz radiation around the plasma channel at $x = 0, \Lambda_0/4, \Lambda_0/2, 3\Lambda_0/4$, where the field strength is normalized by $m_e\omega_0 c/e$ or ~4000 GV/m for a wavelength of 0.8 μm.

of the laser trajectory is decided by the sign of $z_0 \tan\theta_y$. If $z_0 \tan\theta_y > 0$, the laser rotates counterclockwise along the x-axis [as shown in Fig. 1(a)] and vice versa. Assume φ to be the azimuth angle in the y-z plane defined by $\varphi = \tan^{-1}(z/y)$.

2.2 THz Radiation Driven by a Laser Pulse with Twisted Trajectories

With a twisted trajectory as discussed above, the laser centroid keeps away from the channel center and spirals around the central axis of the plasma channel (x-axis) with the same radius $r_{\rm cen}$ during propagation. We consider a weakly relativistic laser $a_L = a_0 \exp(-r_L^2/W_0^2)\sin^2[\pi(x-ct)/d_L]$, where a_0 is related to the peak laser intensity through $I\lambda_0^2 = a_0^2 \cdot 1.37\times10^{18}\ \mathrm{W\,cm^{-2}\,\mu m^2}$, d_L and W_0 are respectively the duration and beam waists of the laser pulse, and $r_L = r - r_{\rm cen}$ is the radial coordinate from the laser centroid. At each position illuminated by the laser pulse, a transverse transient current $\partial J_\perp/\partial t = -\mathrm{enc}^2 a_L^2 r_L/W_0^2$ is excited due to the ponderomotive force[36,37] $F_p = -m_e c^2 \nabla a_L^2/4$. Here, e, m_e, and c are the charge and mass of electrons, and the speed of light in a vacuum, respectively. Within each cross-section along the x-axis as shown in Fig. 1(c), the temporal rate of total transient current $R_J(x) = \int \partial J_\perp/\partial t \mathrm{d}S$ is the spatial summation over the laser beam cross-section. Taking Fig. 1(c1) as an example, one can find that the y-direction component of R_J vanishes as the current in the upper half is equal to that of the lower half with the opposite polarity on r_L. However, the z-direction component accumulates as the right half covers a higher plasma density. Therefore, R_J is aligned in the off-axis direction at each cross-section, which can be derived as

$$R_J(x) = \pm R_{J0}(x)\sin\left(\frac{2\pi}{\Lambda_0}x\right)\hat{y} + R_{J0}(x)\cos\left(\frac{2\pi}{\Lambda_0}x\right)\hat{z}. \quad (1)$$

Here, $R_{J0}(x) = |R_J(x)|$ is the amplitude of the temporal rate of transient current, and $\hat{y}$ and $\hat{z}$ are the unit vectors. The sign of the first term, which is determined by the chirality of the trajectory, is positive if $z_0 \tan\theta_y > 0$, and vice versa. Along with propagation of the laser pulse, the accumulated current at each position shall lead to a THz radiation[38,39] $E_{\rm THz} \propto R_J(x)$, which is polarized at the off-axis direction as well. To ensure that the THz pulses can radiate out of the channel, we consider a channel with a finite radius as shown in Fig. 1(b), where r_c and r_w are the channel radius and channel wall width, respectively. Such a density profile can be obtained experimentally with a tunable r_c in the expansion process of laser-induced plasma waveguides.[40–42]

To investigate the THz radiation as well as the laser dynamics in the plasma channel quantitatively, we conduct 3D PIC simulations using the code OSIRIS.[43] The detailed simulation parameters are given in methods. The trajectories for laser beams propagating inside this plasma channel under two different laser injection conditions are shown in Fig. 2(a). It is clearly shown that the laser centroid follows a spiral trajectory around the channel axis. With the injection condition of $z_0 = 10\,\lambda_0$ and $\theta_y = 88.5$ deg, the trajectory period for the laser spin inside the plasma channel is about $\Lambda_0 = 1.95$ mm, which agrees well with the calculated result of 1.92 mm. Under the laser injection condition of $z_0 = 10\,\lambda_0$ and $\theta_y = 91.5$ deg, the calculated Λ_0 keeps the same value, whereas the chirality of the laser trajectory is reversed clockwise following the sign of $z_0 \tan\theta_y$. The snapshots of the THz electric field around the plasma channel at $x = 0, \Lambda_0/4, \Lambda_0/2, 3\Lambda_0/4$ under the laser injection condition of $z_0 = 10\lambda_0$ and $\theta_y = 88.5$ deg are shown in Fig. 1(d). It is notable that the THz pulse radiates through the plasma-vacuum boundary close to the laser centroid with its polarization parallel to the off-axis direction of the laser centroid. The polarity of the THz radiation changes along the plasma channel. For example, it is reversed for THz emission from the plasma segments separated by $\Lambda_0/2$ along the channel axis, as Fig. 1(d3) compared with Fig. 1(d1) and Fig. 1(d4) compared with Fig. 1(d2). This result is associated with the polarity reversal of $R_J(x)$. Generally, one can say that THz radiation is radially polarized.

2.3 Orbital Angular Momentum Carried by THz Radiation

As given in previous studies,[39] the spatial distribution of THz radiation induced by transverse transient current always keeps a cone. However, as the incident laser beam for driving the THz radiation is non-concentric with the plasma channel, the spatial distribution of the THz radiation is reformed due to its coupling with the plasma wave. As the skin depth of the THz radiation $c/\omega_{\rm THz}$ is in the order of tens of microns, the spatial distribution of the emitted THz pulse is always following the off-axis direction of the beam centroid with respect to the channel center, as schematically shown in Fig. 1(c). The simulation result in Fig. 1(d) confirms our analysis. Provided that the laser beam propagates with a cylindrical spiral trajectory in the plasma

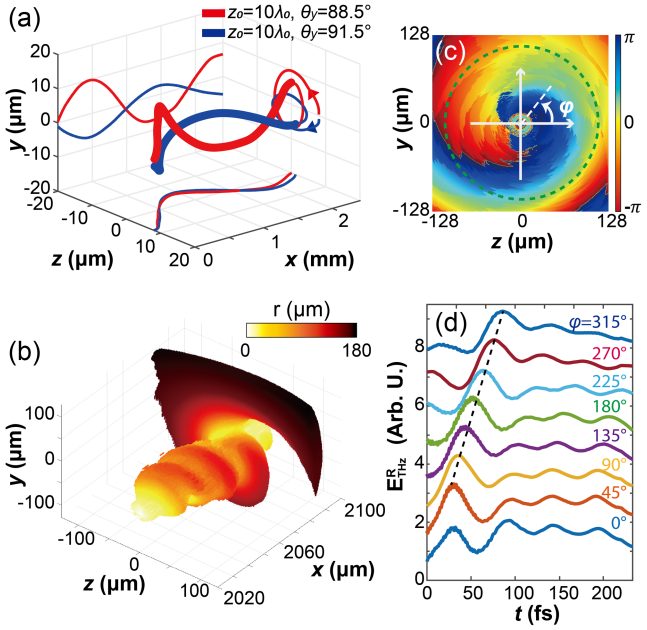

Fig. 2 3D PIC simulation results. (a) Laser trajectories found in the simulation under two different laser injection conditions. The arrows denote the chirality of the trajectories. (b) Contour of the THz radiation. The display threshold of the THz electric field is 7.8 MV/m. The color of the contour is only associated with the position away from the plasma channel center. (c) Phase distribution of the THz radiation collected at $t = 2300\,T_0$. (d) Waveforms of the THz radiation collected at a radius of 100 μm from the channel center [marked in panel (c) as the green dashed circle] for different azimuth angles φ.

channel, the THz pulse radiated from different segments of the channel rotates its radiation direction at far-field as shown in Fig. 1(a). In this case, the THz radiation at a specified azimuth angle φ (clockwise from the z-axis) at the far field is mapped to a specific position along the laser propagation. Therefore, the far-field radiation can be derived as

$$dE_{\mathrm{THz}}(x,R,\varphi) \propto R_J(x)\delta\left(\varphi-\sigma\frac{2\pi x}{\Lambda_0}\right)\cdot\frac{1}{R}e^{ik_{\mathrm{THz}}R}\cdot e^{i\Phi(x)}. \quad (2)$$

Here, δ is the Dirac delta function, $\sigma = z_0 \tan\theta_y/|z_0\tan\theta_y|$, with $z_0\tan\theta_y$ to define the chirality of the trajectory. k_{THz} is the wavevector of the THz radiation, R is the propagation distance to the far field, and Φ is the propagation phase of the THz radiation, which is introduced by the propagation effects of both the laser pulse and the THz radiation.

As for the laser pulse, the optical length dD_{laser} within a plasma segment dx along the propagation axis can be derived as

$$dD_{\mathrm{laser}} = N_p\sqrt{1+(2\pi z_0/\Lambda_0)^2}dx, \quad (3)$$

where N_p is the refractive index of the plasma channel for the laser beam at $r = z_0$, and N_0 is the vacuum refractive index for THz radiation. Considering that the plasma density is in the order of $\sim 10^{18}$ cm^{-3}, which is relatively low compared with the critical density of the drive laser in the order of $\sim 10^{21}$ cm^{-3}, we take the approximation of $N_p = N_0\sqrt{1-\omega_p^2/\omega^2} \approx N_0 = 1$. Moreover, the oblique incident angle of the laser θ_y is close to $\pi/2$, and the off-axis position z_0 should be within the beam radius for stable guiding.[35] Therefore, we employ the first order of Taylor's series in Eq. (3) with the fact that $\Lambda_0 \gg z_0$, and the optical length of the laser within a propagation period Λ_0 can be derived as $D_{\mathrm{laser}} = \Lambda_0(1+1/2\tan^2\theta_y)$. For the radiated THz pulse, it first propagates through the plasma area and then propagates rectilinearly with a radiation angle α [as marked in Fig. 1(a)] after leaving the side edge of the plasma channel. Considering that the critical density of the THz radiation is comparable to the plasma density, the refractive index of the plasma channel for the THz radiation is $N_p^{\mathrm{THz}}(r) = N_0\sqrt{1-\omega_p^2(r)/\omega_{\mathrm{THz}}^2}$. The optical length of the THz radiation D_{THz} within a propagation period Λ_0 can be approximated as

$$D_{\mathrm{THz}} = N_p^{\mathrm{THz}}d/\sin\alpha + N_0(\Lambda_0 - d/\tan\alpha)/\cos\alpha, \quad (4)$$

where $d = r_c + r_w - z_0$ is the transverse distance from the laser centroid to the channel boundary. Considering that different segments of the plasma channel contribute to THz radiation with different spatial angles in the y-z plane in Eq. (2), a continuous phase shift $e^{i\Phi(x)}$ is introduced by spatial separation among THz components emitted from different plasma segments, resulting in a THz beam carrying OAM. Once the spatial delay within a propagation period Λ_0 is comparable to the THz wavelength, the THz pulse should have a corresponding topological charge

$$\ell = -\sigma\frac{D_{\mathrm{laser}} - D_{\mathrm{THz}}}{\lambda_{\mathrm{THz}}}, \quad (5)$$

where λ_{THz} is the peak wavelength of THz radiation. The phase shift now can be represented as $\Phi(x) = 2\pi x\ell/\Lambda_0$. This result indicates that the topological charge of the THz radiation is just decided by the injection condition of the laser as λ_{THz} is associated with z_0.

Based on the above analysis, we reconstruct the THz field (see Figs. S1 and S2 in the Supplementary Material) and conduct 3D PIC simulations to examine the features of the THz pulse. To remove the laser field, the calculated electric field is lowpass filtered with the cutoff frequency at 100 THz. The radial component of THz electric field is extracted from the simulation results through $E_{\mathrm{THz}}^R = E_{\mathrm{THz}}^y \sin\varphi + E_{\mathrm{THz}}^z\cos\varphi$. Note that the plasma density in the simulation is assumed to be preformed; therefore, neither plasma current nor Cherenkov radiation[44–46] is included. The simulated THz radiation under the injection condition of $z_0 = 10\lambda_0$ and $\theta_y = 88.5$ deg is shown in Figs. 2(b)–2(d). The THz radiation from each plasma segment along the plasma channel emits at a given azimuth angle φ, forming a tornado-like wavefront as shown in Fig. 2(b). The central frequency of the THz radiation lies at ~15.75 THz with the corresponding wavelength of 19.05 μm. The radiation angle is 5.3 deg as shown in Fig. 3(b). The calculated topological charge of the THz radiation according to Eq. (5) is $\ell = -0.95$. As shown in the phase distribution of the THz radiation in Fig. 2(c), the THz radiation experiences a continuous phase gradient from $\varphi = 0$ to 2π. Meanwhile, the phase singularity of the THz radiation is non-concentric with the plasma channel due to the fractional topological charge.[36] The waveforms of the THz radiation at a radius of 100 μm from the channel center [green dashed line in Fig. 2(c)] collected at different azimuth angles φ are shown in Fig. 2(d). It is notable that the THz waveform is endowed with a negative phase with an increase in angle φ, which agrees with a negative ℓ.

3 Discussion

3.1 Manipulation of the OAM Carried by THz Radiation

As discussed above, the topological charge ℓ can be totally determined by the laser injection conditions based upon Eq. (5). However, once the transverse position z_0 is changed, the THz central wavelength λ_{THz} and the radiation angle α changes as well following the plasma wavelength[47] of $\sqrt{\pi mc^2/n(r)e^2}$. By conducting a series of 3D PIC simulations, the spectra of the THz emission with laser excitation at different z_0 are shown in Fig. 3(a). In the simulation, the channel radius is expanded simultaneously with z_0 for the same amount to ensure that the laser is well-guided within the plasma channel. The extracted central frequency as well as the radiation angle of the THz radiation under different z_0 is shown in Fig. 3(b), in which both parameters increase with increased z_0. The central frequency of the THz radiation remains higher than the plasma frequency at the laser centroid position [blue solid line in Fig. 3(b)]. That is because the low-frequency components experience severe absorption along the propagation path to the plasma–vacuum boundary. As for the radiation angle, the refractive index has a sharper gradient transversely with higher plasma density with increased z_0. Meanwhile, the refraction-induced radiation angle is enhanced.

Taking the variation in central frequency and radiation angle into account, ℓ can be obtained using Eq. (5) as blue lines in Fig. 3(c). When $z_0 < W_0$, as the frequency of the THz radiation increases, the refractive index N_p^{THz} is much lower than 1, leading to a much shorter D_{THz} and steadily increasing on the value

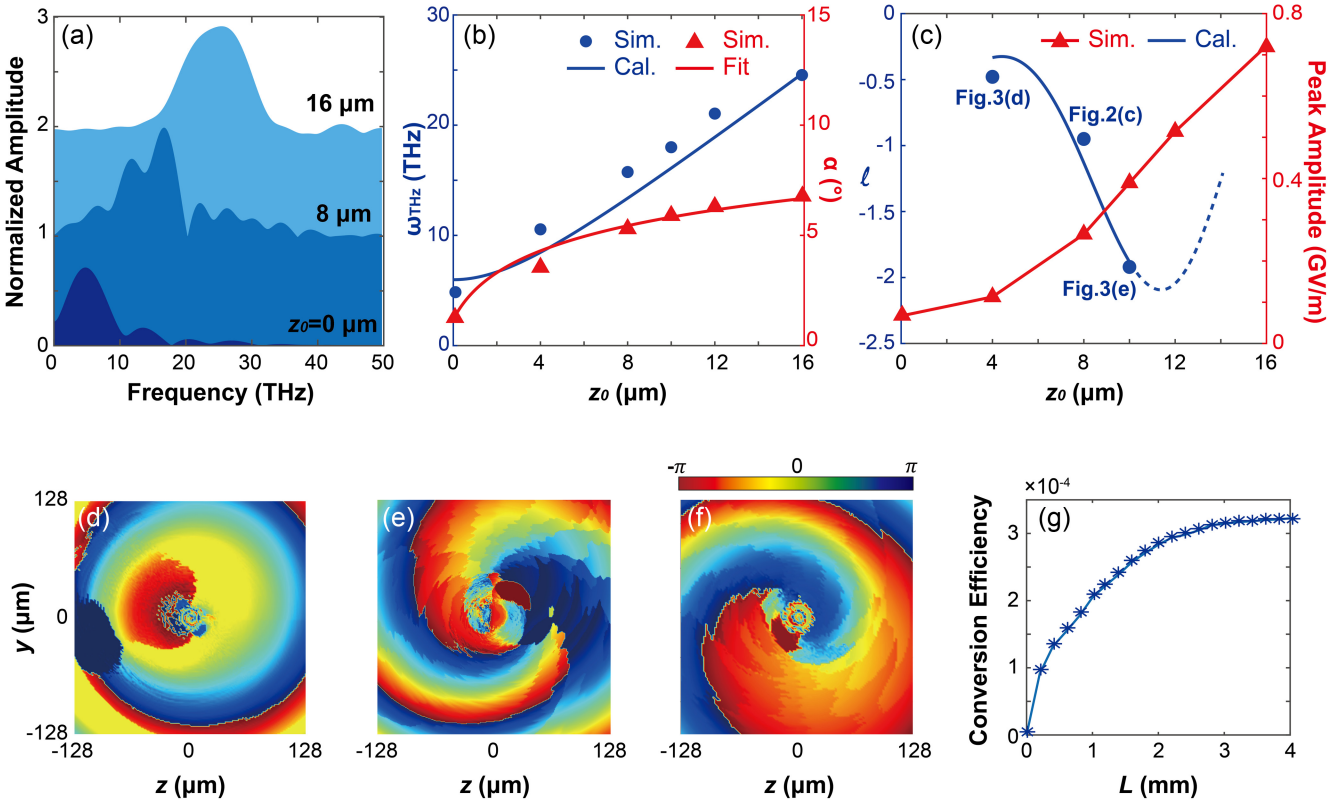

Fig. 3 Manipulation of the OAM of the THz radiation. (a) THz radiation spectra under different offset distances z_0. (b) Simulated THz central frequencies and radiation angles under different z_0 while $\theta_y = 88.5$ deg. The blue solid line gives the calculated plasma frequency at the laser centroid. The red solid line is a fitting of α with $\alpha(\text{deg}) = 4.46\ \text{lg}[z_0 + 0.8\ (\mu\text{m})] + 1.18$. (c) Calculated ℓ utilizing the calculation and fitting lines in panel (b) and the simulated peak amplitude of the THz radiation under different z_0 while $\theta_y = 88.5$ deg. The blue dots give the calculated ℓ with the simulation results in panel (b). (d) Phase distribution of the THz radiation under the injection condition of $z_0 = 5\,\lambda_0$ and $\theta_y = 88.5$ deg. (e) Phase distribution of the THz radiation under the injection condition of $z_0 = 12.5\,\lambda_0$ and $\theta_y = 88.5$ deg. (f) Phase distribution of the THz radiation under the injection condition of $z_0 = 10\,\lambda_0$ and $\theta_y = 91.5$ deg. (g) THz conversion efficiency under the injection condition of $z_0 = 10\,\lambda_0$ and $\theta_y = 88.5$ deg after different propagation lengths L.

of topological charge ℓ. However, as $z_0 > W_0$ with linearly increasing Λ_0, the increased radiation angle becomes non-negligible, leading to a severe increase on the second term of D_{THz} in Eq. (4). Therefore, the value of the topological charge saturates at around -2. Moreover, it is no longer applicable as $z_0 > W_0$ accounting that the calculation [blue dashed line in Fig. 3(c)] employs paraxial approximation.[35] To further increase the order of such THz vortices, one may increase z_0, W_0, and r_0 at the same time.

Based on the above analysis, the order of topological charge on the THz radiation is continuously tunning from -2 to 2, with its chirality decided by the sign of $z_0 \tan\theta_y$. We now give a check on the tunning methods on the topological charge by simulations. Under smaller off-axis quantity conditions, i.e., $z_0 + r_c < c/\omega_p$, the THz can radiate away from the channel at all angles as the distance from the laser centroid to the plasma boundaries is shorter than the skin depth of the THz radiation. The phase distribution of the THz radiation under the injection condition of $z_0 = 4\ \mu$m is shown in Fig. 3(d), in which THz radiation nearly keeps the same phase with different azimuthal angles φ, indicating a tiny topological charge. When z_0 is increased to $10\ \mu$m, the calculated topological charge is $\ell = -1.93$. In this case, the simulation result on the phase distribution of the THz radiation experiences a change of 4π as shown in Fig. 3(d).

As ℓ can be reversed by changing either the sign of z_0 or $\tan\theta_y$ as given in Eq. (5), we now change θ_y to 91.5 deg to flip the sign of $\tan\theta_y$ while keeping z_0 unchanged to get a positive ℓ. As discussed in Fig. 2(a), the chirality of the laser trajectory under this condition was reversed while changing θ_y. The simulation result on the THz phase distribution is shown in Fig. 3(e). Here, the THz radiation gets a positive phase gradient with increasing φ, which corresponds to a THz radiation carrying a reversed OAM compared with Fig. 2(c). These results demonstrate that the OAM of the THz radiation can be flexibly tuned by adjusting the laser injection condition.

3.2 Energy Conversion Efficiency

As discussed in Fig. 1, the energy of the laser wakefield can be continuously converted into THz radiation along the twisted laser trajectory. The THz energy conversion efficiency with

different propagation lengths L is shown in Fig. 3(f). When calculating this, we take only the magnetic field outside the plasma channel area into consideration and low-pass filter components with a frequency above 100 THz. The conversion efficiency here is calculated by dividing the magnetic field energy of the emitted THz emission in vacuum by the magnetic field energy of the input laser. It is shown that conversion efficiency saturates over 3×10^{-4} after propagating for several millimeters for the given off-axis $z_0 = 10\,\lambda_0$. Moreover, a larger off-axis distance z_0 should lead to a stronger THz radiation. As given in Fig. 3(c) (blue line), the peak field strength reaches sub-GV/m under the condition of $z_0 = 16\ \mu$m. In Fig. 2(a), it was shown that the laser trajectory radius keeps decreasing while propagating due to the loss of laser energy by exciting the wakefields. As the skin depth of the THz radiation c/ω_{THz} is in the order of tens of microns, the THz radiation vanishes while the trajectory is shrinking inside. As the off-axis quantity keeps decreasing, the conversion efficiency saturates with a longer propagation distance.

4 Conclusion

We propose a scheme to generate THz vortices with continuously tunable OAM by non-collinearly injecting a weakly relativistic ultrashort laser pulse into a parabolic plasma channel. Such a parabolic plasma channel can be realized experimentally through well-developed technologies, i.e., laser-induced plasma waveguides[40–42] or capillary discharges,[36] and has been widely used in laser–plasma-based electron accelerators.[48,49] The trajectory of the laser beam can be twisted into a cylindrical spiral with a constant radius by manipulating the laser injection conditions. The asymmetric excitation of laser wakefields leads to THz radiation from the side boundary of the plasma channel into the vacuum. Theoretical analysis and 3D PIC simulations reveal that such a THz radiation carries OAM due to the difference in the optical paths between the laser inside the channel and the emitted THz radiation, where its topological charge can be continuously tuned from -2 to 2 by controlling the injection conditions of the injected laser pulse. 3D PIC simulations suggest that the THz vortex pulse can be generated with field strength up to sub-GV/m and energy conversion efficiency over 3×10^{-4} with femtosecond laser pulses at a few tens of mJ in energy. Intense THz vortices with fractional topological charges are unique, and their potential applications are yet to be studied. Such tornado-like electromagnetic pulses should also exist in other frequency bands and could be produced not only in laboratory but also in some astrophysical environments.

5 Appendix A: PIC Simulation Parameters

The 3D PIC simulations are conducted utilizing the code OSIRIS. In the moving frame, the size of the simulation box is $X \times Y \times Z = 100 \times 440 \times 320\lambda_0^3$ with total cells of $2000 \times 880 \times 640$. Note that we rotate the plasma channel for θ_y instead of obliquely injecting the laser beam (see Fig. S3 in the Supplementary Material). In the simulation hereafter, all the results are shown in the channel coordinate for convenience. In the simulation, a_0 is fixed at 0.5 (with the corresponding intensity of $5.35 \times 10^{17}\ \mathrm{W/cm^2}$), and the laser beam radius W_0 and duration d_L are taken as $10\,\lambda_0$ and $20\,\lambda_0$, respectively, where $\lambda_0 = 0.8\ \mu$m is the laser wavelength. The corresponding pulse energy is ~50 mJ with peak power at the terawatt level. The polarization of the laser is fixed in the z-direction. When the plasma channel is matched with the laser beam, one can find that $\Delta n = 1.766 \times 10^{18}\ \mathrm{cm^{-3}} = 10^{-3}\,n_c$ with the channel width $r_0 = 10\,\lambda_0$. We take the minimum density on the channel axis $n_0 = 0.25\,\Delta n$. In the simulation hereafter, r_c and r_w are taken as $17.5\,\lambda_0$ and $5\,\lambda_0$, respectively.

Disclosures

The authors declare no conflicts of interest.

Code and Data Availability

All data needed to evaluate the conclusions are present in this paper and the supplementary material. Additional data related to this paper may be requested from the corresponding authors.

Acknowledgments

This work was supported by the Strategic Priority Research Program of Chinese Academy of Sciences (Grant Nos. XDA25050100 and XDA25010100), the National Natural Science Foundation of China (Grant Nos. 12474428, 12135009, 11991073, and 11991074), and the Science and Technology Commission of Shanghai Municipality (Grant Nos. 22JC1401900 and 24ZR1436900). The authors would like to acknowledge the OSIRIS Consortium, consisting of UCLA and IST (Lisbon, Portugal) for providing access to the OSIRIS 4.0 framework. The authors would also like to acknowledge the π 2.0 cluster of the Center for High Performance Computing at Shanghai Jiao Tong University.

References

1. Y. Fang et al., "Structured electrons with chiral mass and charge," *Science* **385**(6705), 183–187 (2014).
2. F. Nan et al., "Creating stable trapping force and switchable optical torque with tunable phase of light," *Sci. Adv.* **8**, eadd6664 (2022).
3. A. Nicolas et al., "A quantum memory for orbital angular momentum photonic qubits," *Nat. Photonics* **8**, 234–238 (2014).
4. G. Walker et al., "Trans-spectral orbital angular momentum transfer via four-wave mixing in Rb vapor," *Phys. Rev. Lett.* **108**, 243601 (2012).
5. D. Cozzolino et al., "Air-core fiber distribution of hybrid vector vortex-polarization entangled states," *Adv. Photonics* **1**(4), 046005 (2019).
6. B. Ndagano et al., "Characterizing quantum channels with non-separable states of classical light," *Nat. Phys.* **13**, 397–402 (2017).
7. F. Tamburini et al., "Overcoming the Rayleigh criterion limit with optical vortices," *Phys. Rev. Lett.* **97**, 163903 (2006).
8. S. Huang et al., "Spatiotemporal vortex strings," *Sci. Adv.* **10**, eadn6206 (2024).
9. Z. Zhang et al., "Ultrafast control of fractional orbital angular momentum of microlaser emissions," *Light Sci. Appl.* **9**, 179 (2020).
10. G. Tkachenko et al., "Is it possible to create a perfect fractional vortex beam?" *Optica* **4**, 330–333 (2017).
11. H. Zhang et al., "Review on fractional vortex beam," *Nanophotonics* **11**(2), 241–273 (2022).
12. Z. Man et al., "Focal and optical trapping behaviors of radially polarized vortex beam with broken axial symmetry," *AIP Adv.* **7**, 065109 (2017).
13. R. Dasgupta et al., "Optical orientation and rotation of trapped red blood cells with Laguerre-Gaussian mode," *Opt. Express* **19**, 7680–7688 (2011).
14. A. E. Willner et al., "Optical communications using orbital angular momentum beams," *Adv. Opt. Photonics* **7**, 66–106 (2015).

15. Z. Liu et al., "Superhigh-resolution recognition of optical vortex modes assisted by a deep-learning method," *Phys. Rev. Lett.* **123**, 183902 (2015).
16. C. Maurer et al., "What spatial light modulators can do for optical microscopy," *Laser Photonics Rev.* **5**, 81–101 (2011).
17. S. S. R. Oemrawsingh et al., "Experimental demonstration of fractional orbital angular momentum entanglement of two photons," *Phys. Rev. Lett.* **95**, 240501 (2005).
18. Y. Iguchi et al., "Superconducting vortices carrying a temperature-dependent fraction of the flux quantum," *Science* **380**, 1244–1247 (2023).
19. M. Taghinejad et al., "Determining hot-carrier transport dynamics from terahertz emission," *Science* **382**, 299–305 (2023).
20. P. A. Banks, E. M. Kleist, and M. T. Ruggiero, "Investigating the function and design of molecular materials through terahertz vibrational spectroscopy," *Nat. Rev. Chem.* **7**, 480–495 (2023).
21. R. Jia et al., "Valley-conserved topological integrated antenna for100-Gbps THz 6G wireless," *Sci. Adv.* **9**, eadi8500 (2023).
22. C. Zhang et al., "Control of the spin angular momentum and orbital angular momentum of a reflected wave by multifunctional graphene metasurfaces," *Materials* **11**, 1054 (2018).
23. H. Wang et al., "Recent advances in generation of terahertz vortex beams and their applications," *Chin. Phys. B* **29**, 097404 (2020).
24. E. Pickwell and V. Wallace, "Biomedical applications of terahertz technology," *J. Phys. D: Appl. Phys.* **39**, R301 (2006).
25. L. Zhao et al., "Femtosecond relativistic electron beam with reduced timing jitter from THz driven beam compression," *Phys. Rev. Lett.* **124**, 054802 (2020).
26. K. Miyamoto et al., "Direct observation of the topological charge of a terahertz vortex beam generated by a Tsurupica spiral phase plate," *Appl. Phys. Lett.* **104**, 261104 (2014).
27. R. Imai et al., "Generation of broadband terahertz vortex beams," *Opt. Lett.* **39**, 3714–3717 (2014).
28. J. Xie et al., "Integrated terahertz vortex beam emitter for rotating target detection," *Adv. Photonics* **5**(6), 066002 (2023).
29. B. Wang et al., "Generating optical vortex beams by momentum-space polarization vortices centred at bound states in the continuum," *Nat. Photonics* **14**, 623–628 (2020).
30. M. Ivanov et al., "Intensity modulated terahertz vortex wave generation in air plasma by two-color femtosecond laser pulses," *Opt. Lett.* **44**, 3889 (2019).
31. H. Wang et al., "Generation and evolution of different terahertz singular beams from long gas-plasma filaments," *Opt. Express* **29**, 996 (2021).
32. H. Sobhani and E. Dadar, "Terahertz vortex generation methods in rippled and vortex plasmas," *J. Opt. Soc. Amer. A* **36**, 1187 (2019).
33. M. Chen et al., "Tunable synchrotron-like radiation from centimeter scale plasma channels," *Light: Sci. Appl.* **5**, e16015 (2016).
34. A. Butler, D. Spence, and S. Hooker, "Guiding of high-intensity laser pulses with a hydrogen-filled capillary discharge waveguide," *Phys. Rev. Lett.* **89**, 185003 (2002).
35. J. Luo et al., "A compact tunable polarized X-ray source based on laser-plasma helical undulators," *Sci. Rep.* **6**, 29101 (2016).
36. C. Miao, J. P. Palastro, and T. M. Antonsen, "High-power tunable laser driven THz generation in corrugated plasma waveguides," *Phys. Plasmas* **24**, 043109 (2017).
37. L. Zhang et al., "Strong terahertz radiation from a liquid-water line," *Phys. Rev. Appl.* **12**, 014005 (2019).
38. L. Zhang et al., "Observation of terahertz radiation via the two-color laser scheme with uncommon frequency ratios," *Phys. Rev. Lett.* **119**, 235001 (2017).
39. Z. Zhang et al., "Controllable terahertz radiation from a linear-dipole array formed by a two-color laser filament in air," *Phys. Rev. Lett.* **117**, 243901 (2016).
40. L. Feder et al., "Self-waveguiding of relativistic laser pulses in neutral gas channels," *Phys. Rev. Res.* **2**, 043173 (2020).
41. K. Oubrerie et al., "Controlled acceleration of GeV electron beams in an all-optical plasma waveguide," *Light: Sci. Appl.* **11**, 180 (2022).
42. N. Lemos et al., "Plasma expansion into a waveguide created by a linearly polarized femtosecond laser pulse," *Phys. Plasmas* **12**, 070707 (2005).
43. R. A. Fonseca et al., "OSIRIS: a three-dimensional, fully relativistic particle in cell code for modeling plasma based accelerators," *Lecture Notes in Computer Science* **2331**, 342–351 (2002).
44. C. D'Amico et al., "Conical forward THz emission from femtosecond-laser-beam filamentation in air," *Phys. Rev. Lett.* **98**, 235002 (2007).
45. P. Sprangle et al., "Ultrashort laser pulses and electromagnetic pulse generation in air and on dielectric surfaces," *Phys. Rev. E* **69**, 066415 (2004).
46. H. C. Wu et al., "Terahertz radiation from a laser plasma filament," *Phys. Rev. E* **83**, 036407 (2011).
47. L. Wang et al., "Tunable high-field terahertz radiation from plasma channels," *Laser Photonics Rev.* **17**(6), 2200627 (2023).
48. A. J. Gonsalves et al., "Petawatt laser guiding and electron beam acceleration to 8 GeV in a laser-heated capillary discharge waveguide," *Phys. Rev. Lett.* **122**, 084801 (2019).
49. X. Zhu et al., "Experimental demonstration of laser guiding and wakefield acceleration in a curved plasma channel," *Phys. Rev. Lett.* **130**, 215001 (2023).

Linzheng Wang is a postdoc fellow at the Shanghai Jiao Tong University, collaborating with Zhengming Sheng. He received his BS degree in applied physics from Hohai University in 2019 and his PhD in physics from Shanghai Jiao Tong University in 2024. He is the author of tens of papers in journals including *Physical Review Letters*, *Laser & Photonics Reviews*, and *Applied Physical Letters*. He won the U30 Young Scientist/Student Award of the Plasma Branch of the Asia-Pacific Physical Society (AAPPS) in 2024. His current research interests include laser–plasma interactions, plasma-based terahertz radiation, and optical field structuring methods.

Yanping Chen is an associate professor at the School of Physics and Astronomy, Shanghai Jiao Tong University. She received her PhD from Laval University in Canada in 2010 and joined the School of Physics and Astronomy, Shanghai Jiao Tong University, in 2012. Her research mainly includes the development of high-intensity broadband terahertz sources, the development of terahertz pulse control with ultrafast diagnostic technologies, and the exploration of the coherent manipulation mechanism of terahertz pulses on magnetic materials. She has published more than 40 papers in journals such as *Nature Photonics*, *Physical Review Letters*, *Applied Physics Letters*, and *Optics Letters*. "The strong terahertz source with independently controllable polarization states" developed by her team was selected as one of the "Top Ten Advances in Optics of China in 2018." She has trained several doctoral and master's students, among whom some have won the U30 Young Scientist/Student Award of the Plasma Branch of the Asia-Pacific Physical Society, the Wang Daheng University Student Optics Award, the Cai Shidong Plasma Physics Doctoral Dissertation Award, etc.

Min Chen is a professor at the School of Physics and Astronomy, Shanghai Jiao Tong University, specializing in laser–plasma-based particle accelerators and radiation sources. He has published over 150 articles in journals including *Physical Review Letters, Nature Photonics, Science Advances*, etc. He has been funded by the National Outstanding Youth Foundation and won the Outstanding Scientific and Technological Achievement Award (collective) of the Chinese Academy of Sciences (CAS), and the first prize of the Shanghai Natural Science Awards.

Jie Zhang is a professor at Shanghai Jiao Tong University. He is an academician of the CAS, a member of Germany Academy of Sciences

Leopoldina, a fellow of the Third World Academy of Sciences, a foreign member of the Royal Academy of Engineering, and a foreign associate of the American National Academy of Sciences. He was awarded the Edward Teller Medal in 2015 by the American Nuclear Society for his pioneering contribution to laser–plasma physics and high-energy density physics.

Zhengming Sheng is a distinguished professor at the School of Physics and Astronomy, Shanghai Jiao Tong University. He has been focusing on laser–plasma interactions and their applications in inertial confined fusion, generation of advanced radiation sources (terahertz radiation, gamma rays, attosecond pulses, and extremely high-power lasers), advanced plasma-based accelerators, laboratory astrophysics, etc. He has published over 400 peer-reviewed journal papers with over 19,000 Google citations. He received a few awards, including the Fund for Outstanding Young Scholars of NSFC, the Rao Yutai Award of the Chinese Physical Society, the Achievement in Asia Award (AAA Robert T. Poe Prize) of the International Organization of the Chinese Physicists and Astronomers (OCPA), the Shanghai Natural Science Award (first class), and the National Natural Science Award (second class). He is a fellow of the American Physical Society and a fellow of the Institute of Physics, United Kingdom.

Biographies of the other authors are not available.